

On the magnetohydrodynamic modelling of the Crab nebula radio emission

B. Olmi,^{1,2,3★} L. Del Zanna,^{1,2,3} E. Amato,² R. Bandiera² and N. Bucciantini^{2,3}

¹Dipartimento di Fisica e Astronomia, Università degli Studi di Firenze, Via G. Sansone 1, I-50019 Sesto F. no (Firenze), Italy

²INAF – Osservatorio Astrofisico di Arcetri, Largo E. Fermi 5, I-50125 Firenze, Italy

³INFN – Sezione di Firenze, Via G. Sansone 1, I-50019 Sesto F. no (Firenze), Italy

Accepted 2013 November 25. Received 2013 October 30; in original form 2013 July 11

ABSTRACT

In recent years, it has become a well-established paradigm that many aspects of the physics of Pulsar Wind Nebulae can be fully accounted for within a relativistic magnetohydrodynamic description. Numerical simulations have proven extremely successful in reproducing the X-ray morphology of the Crab nebula, down to very fine detail. Radio emission, instead, is currently one of the most obscure aspects of the physics of these objects, and one that holds important information about pulsar properties and their role as antimatter factories. Here, we address the question of radio emission morphology and integrated spectrum from the Crab nebula, by using for the first time an axisymmetric dynamical model with parameters chosen to best reproduce its X-ray morphology. Based on our findings we discuss constraints on the origin of the radio emitting particles.

Key words: acceleration of particles – MHD – radiation mechanisms: non-thermal – pulsars: general – ISM: individual objects: Crab nebula – ISM: supernova remnants.

1 INTRODUCTION

Pulsar Wind Nebulae (PWNe) arise from the interaction of the relativistic wind emanating from a rapidly rotating neutron star with its surroundings. Effective confinement of the pulsar wind by the debris of the parent supernova (SN) explosion induces the formation of a termination shock at which the wind is slowed down and its energy is transformed into that of the magnetized relativistic plasma responsible for the nebular emission. The latter is mostly non-thermal and very broad-band: the class prototype, the Crab nebula, was one of the first synchrotron sources ever identified and shows emission over more than 15 decades in frequency (e.g. Hester 2008).

PWNe collect most of the rotational energy lost by the parent pulsars. As such they are a privileged location to look for answers to old and new questions in pulsar physics. While pulsars are thought to be the primary leptonic antimatter factories in the Galaxy, a big open question concerns the exact amount of pair production in their magnetospheres, the so-called pair multiplicity. In this time of new observational and theoretical developments on the subject, modelling of PWNe is likely to provide the most solid constraints (Bucciantini, Arons & Amato 2011).

In the last few years, the axisymmetric relativistic magnetohydrodynamic (MHD) models of PWNe (Del Zanna, Amato & Bucciantini 2004; Komissarov & Lyubarsky 2004; Del Zanna et al. 2006) have proven extremely successful at accounting for the prop-

erties of these objects as observed in the optical/X-ray band. These models identify in the anisotropy of the pulsar outflow, more energetic in the equatorial plane of the pulsar rotation than along the polar axis, the origin of the jet-torus morphology revealed by *Chandra* in many of these nebulae (Weisskopf et al. 2000; Gaensler & Slane 2006). In addition, they provide a simple explanation for the time variability observed in the inner region of the Crab nebula (Volpi et al. 2008; Camus et al. 2009) and for much of the finer scale structure of the emission.

So far, MHD modelling of PWN radiation has focused on high-energy photons, while completely ignoring the low frequencies, in spite of the fact that the correct interpretation of PWN radio emission is of fundamental importance for understanding many aspects of PWN and pulsar physics. The big question to assess is whether the radio emitting particles are continuously injected in the nebula as part of the pulsar wind and accelerated at the termination shock, or they can rather have a different origin and acceleration site. Indeed, if the radio emitting particles are continuously injected in the nebula together with the optical/X-ray emitting ones, then the inferred pulsar multiplicities are typically larger than current pulsar theories are able to explain (Hibschman & Arons 2001). For example, in the case of the Crab nebula, including low-energy particles in the pulsar outflow one finds the pulsar multiplicity $\kappa \sim 10^6$ and a wind Lorentz factor, averaged over solid angle, $\gamma \sim 10^4$ (Bucciantini et al. 2011). If radio emission comes from particles of a different origin, then, from higher frequency observations, one deduces $\gamma \sim 10^6$ and $\kappa \sim 10^4$ (e.g. Kennel & Coroniti 1984; Gaensler et al. 2002). The value of these two parameters has also important consequences in terms of constraining the acceleration process at

*E-mail: barbara.olmi@unifi.it

work at the wind termination shock (Sironi & Spitkovsky 2011; Arons 2012).

The radio emitting particles, with their large number and long lifetimes against synchrotron losses, could also be relics of earlier times, when the pulsar wind was different from now (Atayan & Aharonian 1996). Or they could come from somewhere else than the pulsar wind, with a possible source being the thermal filaments penetrating the relativistic bubble (e.g. Komissarov 2013). In the latter case, the electrons would have to be accelerated locally to relativistic energies. A possible mechanism to this purpose relies on scattering off local turbulence (Fermi II type process), providing, at the same time, acceleration and spatial diffusion, so as to guarantee a smooth distribution of the radio emission throughout the nebula, despite the presence of enhanced emission associated with the filaments. In the presence of efficient scattering by local turbulence, a rather uniform distribution of particles would also be expected in the case in which the particles are re-accelerated relics, namely they were injected at the termination shock only for a short time during the PWN lifetime, but then re-energized by the interaction with turbulence.

In this paper, we investigate the problem of the origin of radio emitting particles. For the first time, we compute radio emission maps based on the flow structure that arises from the 2D axisymmetric MHD simulation that best reproduces the Crab nebula X-ray emission. We compare the emission morphology under three different hypotheses: (A) assuming that radio particles have always been accelerated at the termination shock; (B) taking their distribution as uniform in the nebula, as could be possibly expected if after being injected, at the shock or by the filaments, they were (re-)accelerated by ambient turbulence; (C) assuming that they were only injected at the termination shock in the nebula for a relatively short time after the SN explosion and with no further re-acceleration.

One piece of information that seems to point towards a common origin of the radio emitting and higher energy particles is the observed continuity of the integrated emission spectrum of the Crab nebula, from which continuity of the spectrum of the emitting particles has traditionally been inferred. For other PWNe, the data are just not good enough to allow us to assess this issue, also due to the scarcity of observations of these objects in the IR and optical band, which is where the transition between different spectral slopes usually occurs. In the presence of a uniform magnetic field strength, as assumed by one-zone models, a smoothly joined emission spectrum between radio and optical implies a smooth spectral distribution of the emitting particles. In the presence of a spatially inhomogeneous field, this is not a straightforward inference, since the volume occupied by particles of different energies is different (larger at lower energies) and so is in principle the field strength. We investigate the paradigm of continuity and smoothness of the particle spectrum in the Crab nebula and show that the IR bump of thermal emission associated with dust could easily hide a possible gap between radio and optical emitting particles.

The paper is organized as follows: in Section 2, we describe the adopted pulsar wind model, the simulation set-up, the assumptions on the particle spectrum, and our procedure to calculate the emission; in Section 3, we present our results and discuss the implications of different models, and we conclude in Section 4.

2 PULSAR WIND MODEL AND PARTICLE EMISSION

The initialization and set-up of our 2D numerical simulations is very similar to that described in our earlier papers: here, we double

the resolution and relax the assumption of symmetry at the equator. The physical domain ranges from $r_{\min} = 0.05$ ly to $r_{\max} = 10$ ly, with logarithmic stretching ($dr \propto r$). The angular domain ranges from 0 to π , with reflection conditions at the polar axis. A spatial grid with 800 cells in the radial direction ($\simeq 350$ points per decade) and 400 cells in the polar angle θ is used. We take $v_\phi = B_r = B_\theta \equiv 0$ and the equation of state for an ideal gas with $\gamma = 4/3$, appropriate for the ultrarelativistic limit.

The simulation box is initially divided into four different regions. From outside in we set up: the fully ionized ISM with $n = 1 \text{ cm}^{-3}$; the cold SN ejecta, with total mass corresponding to $M_{\text{ej}} = 6 M_\odot$ and expansion profile $v \propto r$; a *primordial* hot bubble that during the evolution will merge in the actual PWN (just used for numerical stability: it largely avoids numerical diffusion at the contact discontinuity); the cold, magnetized pulsar wind expanding with a relativistic Lorentz factor $\gamma \equiv \gamma_0 = 100$ and continuously injected from the inner boundary at r_{\min} . This value of γ_0 is much lower than what expected to be appropriate for the Crab pulsar wind (e.g. Kennel & Coroniti 1984), but still high enough to guarantee that the flow is highly relativistic, in which case the post-shock dynamics is independent on the exact value of the Lorentz factor.

The structure of the pulsar wind is crucial in determining the shape of the PWN. We assume an energy flux that roughly depends on space as predicted by *split-monopole* models of the pulsar magnetosphere (Michel 1973), namely $F(r, \theta) = c(nm_e c^2 \gamma_0^2 + B^2/4\pi) \propto r^{-2} \sin^2 \theta$, where $B \equiv B_\phi$ is the embedded toroidal magnetic field and n is the number density of the outflow, but we remark that recent 3D models seem to indicate a different behaviour for oblique rotators ($\sim \sin^4 \theta$) (Spitkovsky 2006; Tchekhovskoy, Spitkovsky & Li 2013). The precise spatial dependence of the energy flux is taken as

$$F(r, \theta) = \frac{L_0}{4\pi r^2} \mathcal{F}(\theta), \quad \mathcal{F}(\theta) = \frac{\alpha + (1 - \alpha) \sin^2 \theta}{1 - (1 - \alpha)/3}, \quad (1)$$

where $L_0 = 5 \times 10^{38} \text{ erg s}^{-1}$ is the pulsar spin-down luminosity, which we take as constant in time, and $\alpha \ll 1$ is the *anisotropy parameter*, which controls the ratio between polar and equatorial energy flux. The magnetic field is assumed as

$$B(r, \theta) = \sqrt{\frac{\sigma_0 L_0}{c}} \frac{\mathcal{G}(\theta)}{r}, \quad \mathcal{G}(\theta) = \sin \theta \tanh \left[b \left(\frac{\pi}{2} - \theta \right) \right], \quad (2)$$

where σ_0 defines the magnitude of B . The function $\mathcal{G}(\theta)$ is chosen having in mind the split-monopole dependence on latitude, but also the fact that the wind is expected to be striped (Coroniti 1990) and dissipation is likely to take place between the stripes within a belt around the pulsar rotational equator. The parameter b relates to the width of this belt: for large values of b the pure split-monopole is recovered, while for $b \sim 1$ dissipation modulates the field strength at all latitudes (Del Zanna et al. 2004). The wind magnetization is defined as $\sigma = B^2/(4\pi n m_e \gamma_0^2 c^2) = \sigma_0 \mathcal{G}^2/(\mathcal{F} - \sigma_0 \mathcal{G}^2)$ and depends on θ alone. Finally, equations (1) and (2) lead to

$$n(r, \theta) = \frac{L_0}{4\pi c^3 m_e \gamma_0^2} \frac{1}{r^2} [\mathcal{F}(\theta) - \sigma_0 \mathcal{G}^2(\theta)]. \quad (3)$$

The synchrotron spectrum of the Crab nebula can be described as produced by particles with a broken power-law distribution in energy (Amato et al. 2000). In the following, we assume that the particles responsible for the optical/X-ray emission are, in all cases, constantly accelerated at the shock, while the radio emitting particles can have different origins: be part of the pulsar outflow and constantly accelerated at the shock (Case A); uniformly distributed in the nebula (Case B); resulting from a burst of acceleration at the

shock, only lasting for a limited time (of the order of 10 per cent of the nebular age), and then advected in the nebula, with no spatial diffusion or further re-acceleration (Case C).

We would like to point out, right from the beginning, that Case C corresponds to a model of relic particles that were injected in the nebula at some early time, when the pulsar was spinning down in a different way, either in terms of overall L_0 or in terms of producing a different multiplicity. This pure relic model, in which the particles are not re-accelerated in the nebula after their initial early injection, is only considered to the purpose of illustrating how the emission morphology would change under this extreme assumption. Indeed, a model of relics that does not conflict with any energetic requirement is likely to give rise to a particle distribution close to that assumed in Case B. Here, the underlying physical picture is that of particles being scattered and accelerated by turbulence in the nebular volume. No matter whether they are extracted from the thermal bath of the filaments or whether they were injected at the shock at early time, the interaction with turbulence that ensures (re)acceleration also smoothes out all the spatial gradients.

Since both model A and B give results in reasonable agreement with the data, in the following we discuss them in parallel, while treating Case C separately.

The general form of the distribution function of newly injected particles in the nebula is given as

$$f_{0s}(\epsilon_0) = (p_s - 1) \frac{K_s}{\epsilon_s^{\min}} \left(\frac{\epsilon_0}{\epsilon_s^{\min}} \right)^{-p_s}, \quad \epsilon_s^{\min} \leq \epsilon_0 \leq \epsilon_s^{\max}, \quad (4)$$

where ϵ is the particle Lorentz factor, K_s a normalization factor, and the extremes of the distribution and the power-law index will be different, depending on whether radio or optical/X-ray emitting particles are considered, and determined from comparison with the data.

The local distribution function of wind particles at any place in the PWN is determined by conservation of particle number along the streamlines, taking into account adiabatic and synchrotron losses

$$f_s(\epsilon) = \left(\frac{n}{n_0} \right)^{4/3} \left(\frac{\epsilon_0}{\epsilon} \right)^2 f_{0s}(\epsilon_0), \quad \epsilon_0 = \left(\frac{n_0}{n} \right)^{1/3} \frac{\epsilon}{1 - \epsilon/\epsilon_\infty}. \quad (5)$$

The factors with n/n_0 take into account the changes in volume of the fluid element, with n the total particle number density, continuously injected in the wind as in equation (3), and n_0 its value immediately downstream of the shock. Here, ϵ_∞ is the maximum particle energy at every point in space–time corresponding to an injection energy $\epsilon_0 \rightarrow \infty$, and is evolved by the code as in Del Zanna et al. (2006).

The densities n and n_0 are evolved in space and time as in Camus et al. (2009), according to the equations

$$\frac{\partial}{\partial t}(n\gamma) + \nabla \cdot (n\gamma \mathbf{v}) = 0, \quad \frac{d}{dt}n_0 \equiv \left(\frac{\partial}{\partial t} + \mathbf{v} \cdot \nabla \right) n_0 = 0, \quad (6)$$

where \mathbf{v} and γ are the flow velocity and Lorentz factor, respectively. The value of n_0 is then used to normalize the distribution function of particles that are of wind origin (Case A): for these we take $K_s = \xi_s n_0$ and determine ξ_s from fitting the data. When we consider Case B, the spatially homogeneous (and constant in time) distribution function of radio particles is simply given as $f_R(\epsilon) = f_{0R}(\epsilon_0)$, with $\epsilon_0 \equiv \epsilon$ and $K_R = n_R = \text{const}$ in equation (4).

Given the local spectrum of the emitting particles, the synchrotron emissivity at all frequencies, surface brightness maps and the integrated spectrum are computed through standard formulas, described in detail in Del Zanna et al. (2006).

3 SIMULATION RESULTS

This section is devoted to comparison of the radio emission morphology resulting from the different assumptions on low-energy particle acceleration illustrated above. We have performed several numerical simulations aimed at determining what values of the dynamical parameters lead to emission maps that most closely reproduce the Crab nebula morphology at high energy. With respect to previous work on the subject (see Del Zanna et al. 2006; Volpi et al. 2008), we have explored a much wider portion of parameter space, including values of σ_0 larger than unity, and also varying, for the first time to our knowledge, the wind anisotropy parameter α . Detailed results of these simulations will be presented elsewhere, while for the current purpose what is important is the identification of the flow parameters that provide the best description of the Crab nebula X-ray morphology. Even if we employ a different simulation set-up, the best set of values for the free parameters is still that found by Del Zanna et al. (2006): $\alpha = 0.1$, $\sigma_0 = 0.025$, $b = 10$. The parameters describing the particle spectrum at the basis of the emission are reported in Table 1, and will be discussed later on.

In Fig. 1, we show the (toroidal) magnetic field at $t = 950$ yr of evolution. The size of the termination shock ($\simeq 0.7$ ly at the equator) and that of the contact discontinuity with the expanding ejecta ($\simeq 7$ ly) are approximately as observed. The field changes polarity around the equator and eddies cause the current sheet to twist and tangle in the downstream, creating a strong mixing of the field (*islands* of opposite polarity can also be seen) and consequent

Table 1. Spectral fit parameters for the two families $f_R(\epsilon_0)$ and $f_X(\epsilon_0)$.

Radio		Optical/X-ray	
Parameter	Value	Parameter	Value
p_R	1.6	p_X	2.9
ϵ_R^{\min}	1.0×10^3	ϵ_X^{\min}	7.0×10^5
ϵ_R^{\max}	2.0×10^5	ϵ_X^{\max}	4.0×10^9
ξ_R	1.7×10^{-2}	ξ_X	2.2×10^{-4}

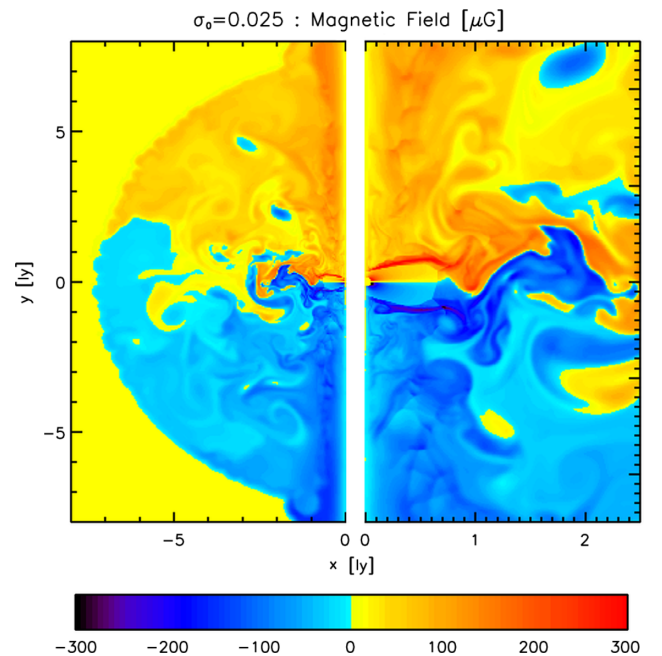


Figure 1. The magnetic field distribution in the simulated nebula.

dissipation (Bucciantini & Del Zanna 2013). The field is lower than expected basically everywhere: well below 10^{-4} G in the external regions and $\simeq 2 \times 10^{-4}$ G just downstream of the termination shock and within a cylindrical region of radius ~ 1 ly around the polar axis (where a jet is present due to magnetic hoop stresses).

3.1 Shock versus distributed particle acceleration

In this subsection, we compare the radio emission morphology resulting from assumptions A and B, namely ongoing acceleration of the low-energy particles at the termination shock, followed by advection with the flow (in perfect analogy with optical/X-ray emitting particles, Case A), or uniform distribution in the whole nebular volume (Case B).

The radio emission maps, which are here computed for the first time on top of MHD simulations, directly reflect the magnetic field structure, and, at some level, the structure of the velocity field (due to Doppler boosting). In the top row of Fig. 2, we show the results of Case A, whereas the lower row pertains to Case B. In the left-hand panels, we report the surface brightness maps at 1.4 GHz. The maps computed under the two different assumptions on the origin and distribution of radio emitting particles are basically identical. Ring-like structures, very similar to those observed in the optical and X-rays are clearly seen at these long wavelengths too. Their appearance is in fact only due to local enhancements in the magnetic field and Doppler boost associated with the local velocity field. In the right-hand panels, we show images obtained by subtracting

two maps computed for epochs that are two months apart: *wisp*-like motion is clearly seen also at radio wavelengths, in perfect agreement with what observed by Bietenholz, Frail & Hester (2001). Again, no substantial difference between the two cases A and B can be noticed, the only discrepancy being due to the central slightly brighter features. Our conclusion is that the appearance of radio *wisps* does not bear any implication on the injection site of the emitting particles, but only on the underlying flow structure.

On the other hand, the emission structure we find appears to be too strongly concentrated in the axial direction in comparison with observations: this is again independent on the assumed spatial distribution of particles in the nebula. One could argue that such an effect is actually present in the real data but masked by the presence of thermal filaments, which give a non-negligible contribution in this band. We compared our results with the map at 1.4 GHz published by Bandiera, Neri & Cesaroni (2002), where subtraction of the filaments was performed. In the central panels of Fig. 2, we show our emission maps smoothed with the same technique and using the same units of mJy arcsec^{-2} as in the cited work for direct comparison. This smoothed maps appear to be very similar to the one based on observations from both a qualitative and quantitative point of view. The computed emission shows a strong cylindrical symmetry, somewhat at odds with the ellipsoidal structure in the data. Once more, results for Cases A and B are nearly undistinguishable.

The reason for the latter discrepancy is likely related to the fact that axisymmetric simulations do not provide a good description of the magnetic field on large scale. Kink-type instabilities, that are

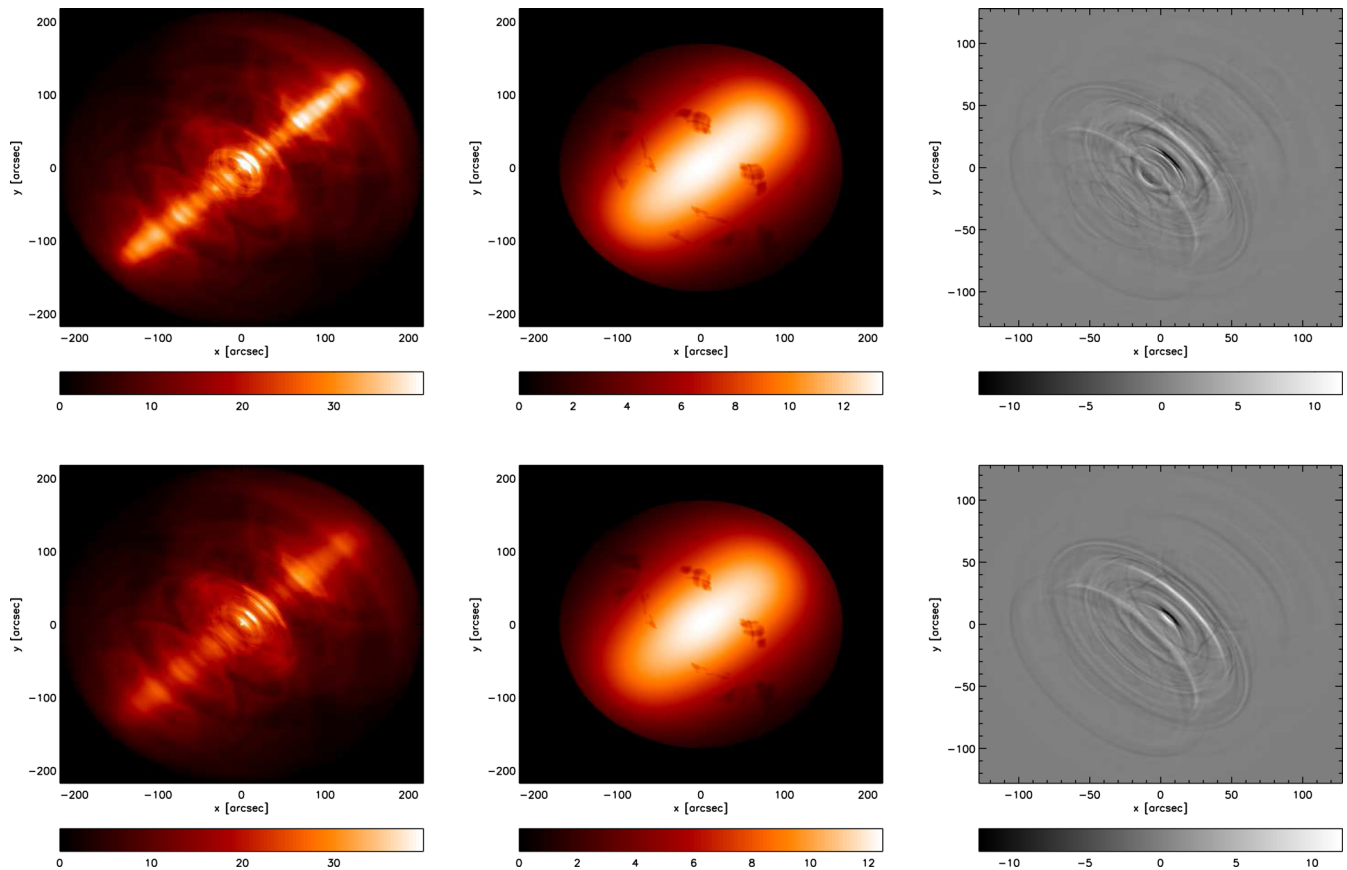


Figure 2. Simulated maps of radio emission and *wisps* at 1.4 GHz, expressed in mJy arcsec^{-2} . *Left-hand panels*: surface brightness maps; *middle panels*: surface brightness maps with subtraction of small scales; *right-hand panels*: *wisps* obtained by subtracting two surface brightness maps with a time separation of two months. The upper row refers to Case A and the lower one to Case B, for which $n_R = 1.4 \times 10^{-6} \text{ cm}^{-3}$.

likely to be at work in these nebulae (Begelman 1998), are artificially suppressed in 2D. This might reflect in a simulated magnetic field that has a much higher degree of order than in reality: the discrepancy will become more apparent in the emission the further one moves from the central pulsar, so that the instabilities have time to grow. This fact makes the radio emission the most sensitive probe of such an effect, and at the same time it explains why with axisymmetric simulations we are able anyway to reproduce the high-energy morphology: the short lifetimes of optical/X-ray emitting particles keeps them confined within a region where a perfectly toroidal magnetic field is still not such a bad approximation. An additional hint to such an effect comes from the observation that in order to reproduce the observed brightness contrast between the inner ring and torus at X-ray frequencies the emission must be computed assuming that the underlying magnetic field progressively becomes isotropic with increasing distance from the termination shock: the ring is otherwise too bright.

The artificially high degree of order of the magnetic field is obviously accompanied by important dynamical consequences. The associated hoop stresses are also larger than in reality and might be forcing us to adopt an artificially small value of the magnetization in our simulations. Strong suggestions that this is the case also come from Fig. 3, where we plot the integrated emission spectrum of the Crab nebula as computed based on our simulation, and we compare it with multiwavelength observations. The particle distribution functions adopted are as described in Section 2 with the parameters given in Table 1. In spite of the good fit of the synchrotron part of the spectrum, the exceedingly low magnetic field strength in the nebula is revealed by a careful inspection of the fit parameters: the spectrum of optical/X-ray emitting particles that is required to reproduce the observations is very steep (see Table 1), with a slope of $p_X = 2.9$, to be compared with the value $p_X = 2.2$ that is deduced from observations of the inner nebula (Veron-Cetty & Woltjer 1993; Mori et al. 2004).

This is due to the fact that synchrotron losses are too weak in our simulation and do not provide sufficient softening of the injected particle distribution, so that we are forced to assume a steep injection spectrum in order to reproduce the high energy observations. However, this becomes even more apparent from the gamma-ray flux due to the Inverse Compton (IC) contribution, which, when calculated self-consistently by integrating over the whole nebular volume, is higher by a factor ~ 3 compared to observations. This is precisely the discrepancy we have in the average magnetic field value: in order to reproduce the synchrotron spectrum we are forced to inject more particles in the PWN, leading to a higher IC flux. This was

already found and described in details by Volpi et al. (2008): very similar findings apply to the simulations with the present settings.

Finally, let us comment on the properties of the particle distribution function underlying the emission, focusing on Case A. This case corresponds to the spectrum described in Table 1 and Fig. 3 (right-hand panel). First thing to notice is that the spectrum of emitting particles we adopt has a gap between the radio and the X-rays. The size of the gap is not well established from our fit: anything between no discontinuity ($\epsilon_r^{\max} = \epsilon_X^{\min}$) and a discontinuity extending to an energy a factor of 3–4 lower than ϵ_X^{\min} works well (the ratio for our best fit is 3.5). This result is obtained with sharp cut-offs in the particle spectra both at high and low energy, while with exponential cut-offs larger gaps would be allowed. In addition, our best fit corresponds to a discontinuous distribution at injection, in the sense that the two curves do not match in the gap region and that extrapolation of the low-energy spectrum to ϵ_X^{\min} would give half of the particles that are actually required at this energy. However, this discrepancy should not be trusted because, as already discussed, inference of the particle spectrum depends on the magnetic field strength and profile, and we know that in reality this will be different than in our current axisymmetric simulations. Indeed, the spectra described in Table 1 correspond to conversion into accelerated particles of a fraction larger than one of the pulsar spin-down luminosity.

3.2 On the variability of radio ‘wisps’

We have seen in the previous subsection that radio *wisps* are easily reproduced by our relativistic MHD model. Here, we investigate their variability properties following the analysis by Bietenholz et al. (2004). These authors studied long-term variability of the radio emission component through observations during an ~ 3 yr period, together with much shorter term variations (time-scale of a few months) in the innermost region of the nebula. For direct comparison with this analysis of time-variability, we use maps that are computed at 5 GHz, instead of the previously used frequency of 1.4 GHz. As above, the difference images are obtained by subtraction. We only discuss maps corresponding to Case B, since those for Case A are very similar.

In Fig. 4, the radio emission difference maps at 5 GHz are shown: the long term is shown in the left-hand panel, short term in the right one. As one can expect, the right-hand panel corresponds to the radio *wisp*-like structures in the inner region of the nebula, just as in the maps at 1.4 GHz already shown (images on the right in Fig. 2). As far as the long-term map is concerned, the first thing to notice is that a significant component of the variability has a time-scale

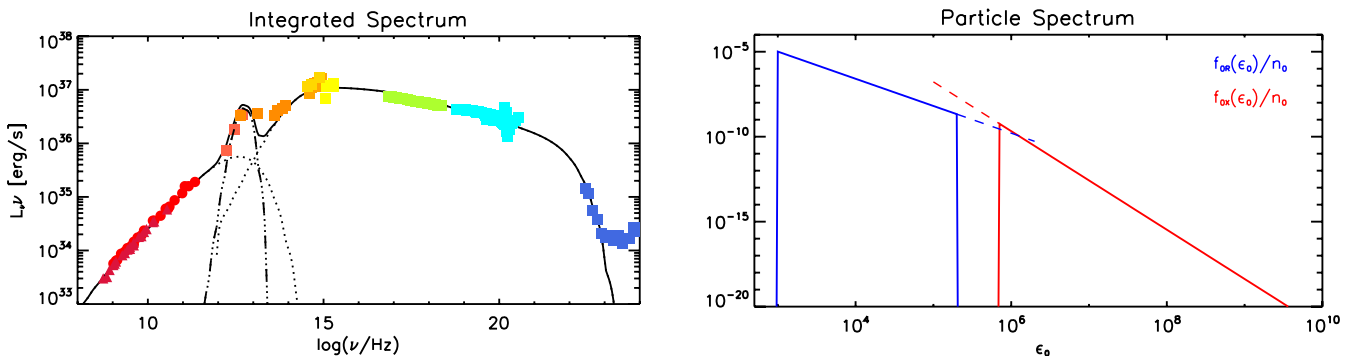


Figure 3. The Crab nebula integrated synchrotron spectrum. Data are taken from Meyer, Horns & Zechlin (2010). Dotted lines indicate the contributions from the two families of emitting particles, whereas the solid one represents the total spectrum. The injection spectra are shown in the right-hand panel for the case of radio particles of wind origin (Case A). The left (radio particles) and right curve (optical/X-ray) correspond to the parameters in Table 1.

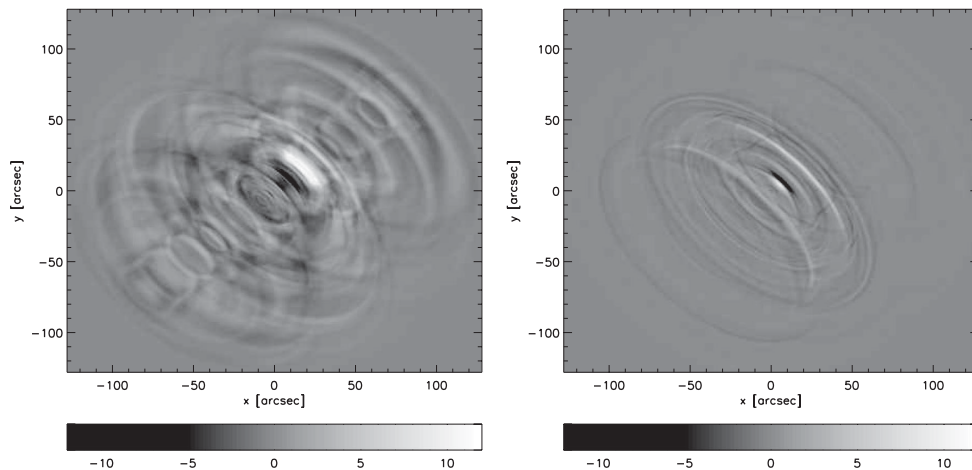


Figure 4. Changes occurring in the nebula on a 3 yr time-scale (*left-hand panel*) and on ~ 2 months (*right-hand panel*), at 5 GHz. Moving ripples and arc-like structures are well visible in both images. On the x and y axes the distance from the central pulsar in arcsec is reported. The two maps are expressed in mJy arcsec^{-2} .

longer than that of the *wisps*. The region that shows long-term variability extends for ~ 3 ly around the pulsar, namely it is twice as large in linear size as the region showing short-term variability. Additional remarkable features in the image on the left of Fig. 4 are elliptical arcs, found in the central zone and characterized by an outward motion, similar to the optical/X-ray *wisps*; arc-shaped features that are visible in the body of the nebula, are not centred on the pulsar position and move outwards more slowly than the former (Weisskopf et al. 2012; Schweizer et al. 2013). The inferred projected speed for the inner *wisps* is $\sim 0.4c$ while for the outer moving features is $\sim 0.002c$, as expected from the data analysis.

All these features were found in the data analysis by Bietenholz et al. (2004) and are well reproduced by our axisymmetric model both in shape and associated velocity. We stress again the conclusion that the appearance of *wisps* simply reflects the underlying structure of magnetic and velocity field (due to Doppler boosting). The result is not much affected by the different spatial distribution of the particles in the two cases A and B: indeed, even in the case of acceleration at the shock and following advection (A), thanks to their long lifetimes, the radio particles are everywhere in the Nebula and strong gradients are absent.

3.3 Pure ‘relic’ particles: no re-acceleration

In this section, we discuss what we had defined as our Case C. We consider a model in which radio emitting particles are pure relics: they are injected at the termination shock (as the optical/X-ray emitting one) but only at early times after the SN explosion. The injection of low-energy particles is then halted after a certain time $t_b \ll t_{\text{act}} \simeq 950$ yr, while continuing for the higher energy ones. After injection all particles evolve due to synchrotron and adiabatic losses, while advected with the flow. This time-dependent injection model is meant to represent a sort of primordial *burst*, possibly associated with a different *behaviour* of the pulsar in its early stages, when the spin-down luminosity was almost an order of magnitude greater than the current one (Atoyan 1999): what we have in mind is in fact a higher multiplicity at early times. Our attention is then focused on the final spatial distribution of the radio particles and on the resulting emission map.

Also for the present Case C the simulation set-up is the same as before, except for the particle tracers that are now defined only

for the radio population, with the new value of the maximum local energy set as $\epsilon_\infty = 10^6$.

This value is chosen in order to guarantee a proper representation of the radio emission spectrum. In Section 3, we found that the radio spectrum is currently produced by particles with energy up to a cut-off $\epsilon_b \simeq 2 \times 10^5$. The most recent radio particles were injected in the nebula at the time t_b corresponding to the end of the burst. Since then they have been losing energy due to adiabatic, and, initially, also synchrotron losses: at early times the average magnetic field in the nebula was larger than its current value making synchrotron losses important also for 100 GeV particles. This fact actually constrains the burst duration: if we want the current spectrum of radio emitting particles to still extend up to the value of ϵ_b mentioned above, we require that the burst must have lasted at least for a time:

$$t_b \gtrsim \sqrt{\frac{\epsilon_b \sigma_T c t_{\text{act}}^3 B_{\text{act}}^2}{18\pi m_e c^2}} \sim 80 \left(\frac{\epsilon_b}{2 \times 10^5} \right)^{1/2} \left(\frac{B_{\text{act}}}{50 \mu\text{G}} \right) \text{yr}, \quad (7)$$

where we have used standard synchrotron formulae and approximated the time evolution of the average magnetic field strength as $B(t) \propto t^{-1}$ (Pacini & Salvati 1973). Since the average magnetic field in our simulation at the current age of the Crab nebula is $B_{\text{act}} \sim 50 \mu\text{G}$, we take $t_b = 100$ yr.

We would like to point out however, that if the magnetic field in our simulation were closer to more realistic values (values in agreement with high energy spectral modelling), and hence, a factor 2–5 larger, the lower limit on the burst duration would have been proportionally larger. Therefore, in reality, the highest energy radio emitting particles must have been injected in the nebula no earlier than ~ 500 yr ago, which makes one wonder what might have caused a sudden change in the pulsar multiplicity or spin-down properties long after birth.

In Fig. 5, we show the density tracer at different times (left and middle panels) and the radio surface brightness map at $t = 1000$ yr (right-hand panel). In the image on the left, the density of radio particles is shown at the final stage of injection ($t = t_b$), and its spatial distribution appears almost uniform in the nebula. The middle panel refers to the final stage of evolution, $t \simeq 1000$ yr, and two main differences are evident compared to the first map: the mean value is decreased by about three orders of magnitude and its distribution is not uniform anymore. The lower value of the density results from the adiabatic expansion of the nebular volume.

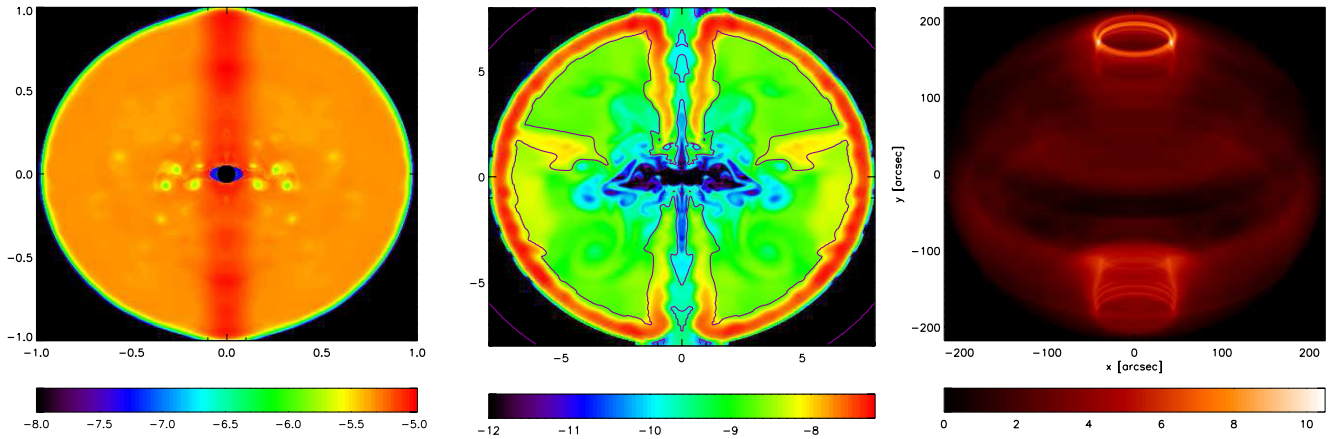


Figure 5. Radio particle density maps at $t = t_b = 100$ yr (left-hand panel) and at $t = 1000$ yr (middle panel); both maps are in logarithmic scale and on the x and y axes the radial distance from the pulsar is reported in ly. The line contour in the second map traces the high-density region in the dynamic density map at the same stage of evolution, connected to the high-density region in the tracer map: see text for more details. Right-hand panel: surface brightness map at 1.4 GHz, in linear scale and normalized at the maximum value.

Furthermore, notice that a sort of higher density shell is visible at the outer edge of the nebula. This is caused by the accumulation of part of the dynamical mass density in that region in the early stages of evolution. Then vortices develop in the nebular flow pattern that confine the circulation in the body of the nebula, preventing new material from reaching the outer shell. As a consequence, the material that settled down there at the beginning does not get mixed anymore. The density of radio particles behaves exactly as mass density and this is the reason for the pattern that we observe in the figure. The same mechanism is at the base of the high-density *fingers* in the NW and NE regions of the nebula.

The line contour in the middle panel of Fig. 5 identifies the region of high-mass density concentration. The radio surface brightness map in the right-hand panel of Fig. 5 is computed with that region subtracted. In order to allow for direct comparison with the spatial distribution of particles, the emission map is not rotated in the plane of the sky, while is inclined with respect to the line of sight, so as to correctly take into account Doppler boosting. Despite having removed most of the spurious effects of numerical origin, the emission morphology is clearly discrepant with respect to observations. The emission is diffuse, but the central region is much darker than observed. While the ring-like structures in the outer region of the nebula are likely related to residual spurious features near the impact regions of the jet, the absence of ‘wisp-like’, Doppler-boosted structures in the inner region is a real difference between this map and the ones shown in the left-hand panel of Fig. 2. This difference arises from the fact that there are no radio emitting particles left at the current time in the innermost region of the nebula, where the field strength is highest and the flow is most dynamic and with the fastest speed.

We have also tried different durations of the burst, while with shorter durations the emission spectrum does not extend to sufficiently high energies, a factor 2–3 longer duration leads to qualitatively similar results. What we learn from this simple model, then, is that the radio particles cannot be described as a relic population of pulsar origin without including a local re-acceleration mechanism in the nebula.

4 COMMENTS AND CONCLUSION

The axisymmetric MHD modelling of the dynamics of PWNe is generally regarded as very successful. In this paper, we point out

some of the limits it shows when its predictions are compared quantitatively with multiwavelength observations of the Crab nebula, the class representative that offers, thanks to the abundance of data, the tightest constraints. The striking agreement between the simulated and observed high-energy morphology of the Crab nebula suggests indeed that the flow structure in the inner regions of this object must be very close to what our simulations predict (Del Zanna et al. 2006). On the other hand, the same comparison suggests that the magnetic field cannot be perfectly toroidal all the way to the outer boundary of the nebula: some degree of turbulence is required in order to reproduce the brightness contrast between the *Chandra* inner ring and torus. This could result from the development of kink instabilities that are artificially suppressed in our 2D simulations, and the same could be responsible for reducing the hoop stress that forces the wind magnetization estimated in 2D to very low values. This very low magnetization is in fact incompatible with the integrated emission spectrum, as already highlighted by Volpi et al. (2008): reproducing the synchrotron part of the spectrum requires conversion into accelerated particles with efficiencies larger than one, and the IC part cannot be reproduced at all. This fact actually prevents us from drawing firm conclusions on the overall particle spectrum underlying the nebular emission.

Recent works about current driven instabilities in 3D (Mizuno et al. 2011; Mignone et al. 2013) confirm the formation of kinks in jets, though the flow arising from the termination shock and the hoop stresses in the nebula itself are not taken into account. Preliminary work with full 3D relativistic MHD modelling of the entire system (Porth, Komissarov & Keppens 2013a,b) seems to finally provide a solution to the long-standing σ paradox: since magnetic flux can be effectively destroyed in the body of the nebula, thanks to the development of kink instabilities, even an ultrarelativistic pulsar wind at equipartition allows for the formation of a PWN with features similar to those observed in the Crab nebula, although the jets are now very weak and almost invisible. Whether all problems of PWN modelling are solved by moving from a 2D to a 3D relativistic MHD description is too early to assess. Current 3D simulations only extend for a very short time (~ 70 yr) after the SN explosion, and at the end of the simulation the self-similar expansion phase has not been reached yet. Even more critical in our view is the fact that the average magnetic field in the nebula is already around $100 \mu\text{G}$ at this very young age, and likely to decrease by a factor larger than 10 by the time the simulated nebula gets to

the Crab current age. No strong conclusions can be drawn at this stage.

The novelty of this work resides in the first attempt ever at a detailed study of the low-energy emission within the framework of 2D MHD. The main conclusion is that the radio emission morphology is basically insensitive to the spatial distribution of the particles in the two scenarios that see them either advected with the flow from the pulsar wind termination shock, or uniformly distributed in the nebula. Not only the surface brightness maps are basically identical, but also moving *radio wisps* appear in both cases, and actually both the innermost fast moving features and the larger scale slower ones, in agreement with the observations by Bietenholz et al. (2004). In terms of variability, we compared the results of our simulations with the cited observations. The fact that the variable structures are well reproduced in our simulations independently of the spatial distribution of the particles points towards the conclusion that these details cannot really prove the origin of the radio emitting particles.

The only scenario that can be excluded is one in which the low energy particles are ‘pure relics’, injected at early times after the SN explosion and then evolved in the absence of further acceleration and spatial diffusion. We were able to directly prove that this scenario does not work in the case of particle injection for less than 400 yr during the history of the nebula. In reality, the requirement on the last episode of acceleration of radio emitting particles would be even more stringent (closer in time episode) if the magnetic field in the simulated nebula were higher. In summary, radio emitting particles could only be fossil in terms of their injection in the nebula, but not in terms of their acceleration history.

As far as acceleration mechanisms are concerned, apart from shock acceleration, the low-energy particles could, in principle, be re-accelerated (if coming from the shock, or accelerated if coming from the thermal filaments) by distributed turbulence in the nebula, either of kinetic origin, injected by the higher energy population of particles, or of MHD origin. Two main sources can be envisioned for the latter: the highly dynamical behaviour of the shock front and nearby eddies where small-scale flows easily form and have been even invoked as sources of the gamma-ray flaring activity (Komissarov & Lyutikov 2011), or the growth of local Kelvin–Helmholtz MHD instabilities at the shear layers of neighbouring *wisps* (Bucciantini & Del Zanna 2006). Another possibility, actually supported by the results of Porth et al. (2013a) is that effective magnetic reconnection in the body of the nebula might also provide particle acceleration: this hypothesis is particularly attractive also because this mechanism naturally seems to provide flat energy spectra, just as generally inferred for young PWNe.

The possibility of explaining radio observations without requiring that the radio emitting particles must be part of the pulsar wind relaxes somewhat the strong requirements on the multiplicity of the Crab pulsar found by Bucciantini et al. (2011). However, explaining the very large number of these particles is still problematic and deserves further investigation. If they are of pulsar origin, then the pulsar multiplicity must have been high at some point in time, and then have possibly decreased to accommodate for current observations of X-ray emitting particles. On the other hand, the radio emitters could also be produced elsewhere in the nebula, for example in the thermal filaments due to Rayleigh–Taylor instabilities (Bucciantini et al. 2004), in which case they would only be electrons rather than pairs. In this case, contrary to recent claims (Blasi & Amato 2011), PWNe could not be responsible for the *positron excess* recently detected (PAMELA Collaboration 2009; AMS-02 Collaboration 2013, for a review see also Serpico 2012).

This explanation is not very appealing, especially because very similar radio spectra are observed in bow-shock PWNe (e.g. Ng et al. 2012), and in these sources the particles are extremely unlikely to come from anywhere else than the pulsar.

REFERENCES

- Amato E., Salvati M., Bandiera R., Pacini F., Woltjer L., 2000, *A&A*, 359, 1107
- AMS-02 Collaboration, 2013, *Phys. Rev. Lett.*, 110, 141102
- Arons J., 2012, *Space Sci. Rev.*, 173, 341
- Atayan A. M., 1999, *A&A*, 346, L49
- Atayan A. M., Aharonian F. A., 1996, *MNRAS*, 278, 525
- Bandiera R., Neri R., Cesaroni R., 2002, *A&A*, 386, 1044
- Begelman M. C., 1998, *ApJ*, 493, 291
- Bietenholz M. F., Frail D. A., Hester J. J., 2001, *ApJ*, 560, 254
- Bietenholz M. F., Hester J. J., Frail D. A., Bartel N., 2004, *ApJ*, 615, 794
- Blasi P., Amato E., 2011, in Rea N., Torres D. F., eds, *Astrophysics and Space Science Proceedings, High-Energy Emission from Pulsars and their Systems: Proceedings of the First Session of the Sant Cugat Forum on Astrophysics*. Springer-Verlag, Berlin, p. 624
- Bucciantini N., Del Zanna L., 2006, *A&A*, 454, 393
- Bucciantini N., Del Zanna L., 2013, *MNRAS*, 428, 71
- Bucciantini N., Amato E., Bandiera R., Blondin J. M., Del Zanna L., 2004, *A&A*, 423, 253
- Bucciantini N., Arons J., Amato E., 2011, *MNRAS*, 410, 381
- Camus N. F., Komissarov S. S., Bucciantini N., Hughes P. A., 2009, *MNRAS*, 400, 1241
- Coroniti F. V., 1990, *ApJ*, 349, 538
- Del Zanna L., Amato E., Bucciantini N., 2004, *A&A*, 421, 1063
- Del Zanna L., Volpi D., Amato E., Bucciantini N., 2006, *A&A*, 453, 621
- Gaensler B. M., Arons J., Kaspi V. M., Pivovarov M. J., Kawai N., Tamura K., 2002, *ApJ*, 569, 878
- Gaensler B. M., Slane P. O., 2006, *ARA&A*, 44, 17
- Hester J. J., 2008, *ARA&A*, 46, 127
- Hibschman J. A., Arons J., 2001, *ApJ*, 560, 871
- Kennel C. F., Coroniti F. V., 1984, *ApJ*, 283, 694
- Komissarov S. S., 2013, *MNRAS*, 428, 2459
- Komissarov S. S., Lyubarsky Y. E., 2004, *MNRAS*, 349, 779
- Komissarov S. S., Lyutikov M., 2011, *MNRAS*, 414, 2017
- Meyer M., Horns D., Zechlin H.-S., 2010, *A&A*, 523, A2
- Michel F. C., 1973, *ApJ*, 180, L133
- Mignone A., Striani E., Tavani M., Ferrari A., 2013, *MNRAS*, 436, 1102
- Mizuno Y., Lyubarsky Y., Nishikawa K.-I., Hardee P. E., 2011, *ApJ*, 728, 90
- Mori K., Burrows D. N., Hester J. J., Pavlov G. G., Shibata S., Tsunemi H., 2004, *ApJ*, 609, 186
- Ng C.-Y., Bucciantini N., Gaensler B. M., Camilo F., Chatterjee S., Bouchard A., 2012, *ApJ*, 746, 105
- Pacini F., Salvati M., 1973, *ApJ*, 186, 249
- PAMELA Collaboration, 2009, *Nature*, 458, 607
- Porth O., Komissarov S. S., Keppens R., 2013a, *MNRAS*, 431, L48
- Porth O., Komissarov S. S., Keppens R., 2013b, preprint ([arXiv:1310.2531](https://arxiv.org/abs/1310.2531))
- Schweizer T., Bucciantini N., Idec W., Nilsson K., Tennant A., Weisskopf M. C., Zanin R., 2013, *MNRAS*, 433, 3325
- Serpico P. D., 2012, *Astropart. Phys.*, 39, 2
- Sironi L., Spitkovsky A., 2011, *ApJ*, 741, 39
- Spitkovsky A., 2006, *ApJ*, 648, L51
- Tchekhovskoy A., Spitkovsky A., Li J. G., 2013, *MNRAS*, 435, L1
- Veron-Cetty M. P., Woltjer L., 1993, *A&A*, 270, 370
- Volpi D., Del Zanna L., Amato E., Bucciantini N., 2008, *A&A*, 485, 337
- Weisskopf M. C. et al., 2000, *ApJ*, 536, L81
- Weisskopf M. C., Elsner R. F., Kolodziejczak J. J., O’Dell S. L., Tennant A. F., 2012, *ApJ*, 746, 41